

# Free Surface Waves for a Lamb–Oseen Vortex Flow

E. Zuccoli<sup>1</sup>, E. J. Brambley<sup>1,2†</sup> and D. Barkley<sup>1</sup>

<sup>1</sup>Mathematics Institute, University of Warwick, UK

<sup>2</sup>WMG, University of Warwick, UK

(Received xx; revised xx; accepted xx)

Surface waves have been observed to rotate around the cores of vortices generated in a swimming pool. To investigate this effect, we have numerically studied the free-surface response of a Lamb–Oseen vortex to small perturbations. The fluid has finite depth but is laterally unbounded. The numerical method used is spectrally accurate, and uses a novel non-reflecting buffer region to simulate a laterally unbounded fluid. While a variety of linear waves can arise in this flow, we focus here on the surface gravity waves observed in the swimming pool. We investigate the linear stability of the vortex as a function of the perturbation azimuthal mode number and the vortex rotation rate. We find that at low rotation rates, linear modes decay by radiating energy to the far field, while at higher rotation rates modes become neutrally stable and trapped in the vicinity of the vortex. In analogy to a quantum-mechanical system, such states correspond to quasi-bound states, i.e., normal modes whose decay rate in time is null and whose corresponding eigenfunctions remain trapped. Quasi-bound states have previously been seen in shallow water surface waves due to small perturbations of a bathtub vortex, although the situation considered here is qualitatively different owing to the lack of an inward flow. We find that for slow vortex rotation rates, waves propagate in the opposite direction to the base flow, whereas, above a threshold rotation rate, waves start co-rotating with the flow as they are dragged along by the vortex.

**Key words:** Surface gravity waves; Waves in rotating fluids.

---

## 1. Introduction

Rotating flows are rather ubiquitous in nature. Examples range from domestic flows such as the bathtub vortex, to geophysical flows and Jupiter’s Great Red Spot, to astrophysical flows such as accretion disks. Rotating flows support the propagation of many different type of waves. These are often viewed as small perturbations to an equilibrium state, also known as a base flow, and the behaviour of such waves depends both on the particular velocity field of the base flow and on the geometry of the problem under consideration. One important class of such waves are interfacial surface waves. These are waves forming at the interface between two fluids with different physical properties, and often are strongly localized close to the interface.

In the present paper, we will study free surface waves on rotating fluid whose velocity

† Email address for correspondence: E.J.Brambley@warwick.ac.uk

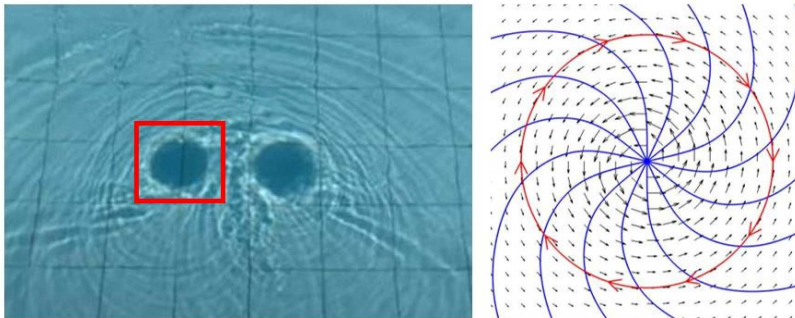


FIGURE 1. The physical scenario motivating this work. Surface waves are trapped within a rotating vortex flow, but propagate in the direction opposite the direction of rotation. Left: Photograph of two vortices in a swimming pool (taken from Skipp 2020). Right: schematic of the flow and surface waves on the left-hand vortex. Black arrows show the base velocity field. Blue lines show the wave crests. Red arrows show the direction of propagation of the waves.

$\mathbf{U}_0$  is that of a Lamb–Oseen vortex

$$\mathbf{U}_0 = \hat{\boldsymbol{\theta}} \frac{\Gamma_0}{2\pi r} \left(1 - \exp\{-r^2/a^2\}\right), \quad (1.1)$$

where  $r$  is the horizontal distance from the vortex centre,  $\hat{\boldsymbol{\theta}}$  is a unit vector in the direction of rotation, and  $\Gamma_0$  and  $a$  are constants (see, e.g. Drazin & Riley 2006, for details of the derivation of this flow). The Lamb–Oseen vortex is in fact an exact solution to the viscous Navier–Stokes equations if we take  $a^2 = 4\nu t$ , where  $\nu$  is the kinematic viscosity, although for short timescales compared with the viscous diffusion timescale,  $a$  may be approximated as constant. Unlike the bathtub vortex, this base flow is entirely independent of height, and is not the result of vortex stretching by a downwards outflow. In that regard, it is more similar to a geophysical vortex, although here we do not consider a stratified atmosphere, nor do we assume the layer of fluid to be thin. In fact, our initial motivation was out of curiosity concerning vortices and waves interacting in a swimming pool. Changes in the surface height can be easily visualized by light and dark patterns on the swimming pool floor (for which the authors recommend a warm sunny climate and an outdoor swimming pool). An “experiment” (Skipp 2020) showed surface waves that appear trapped in the vortex, but which propagate around the vortex in the opposite direction to the vortex flow. A photograph of the phenomena, together with a schematic representation, is shown in figure 1.

Free surface rotating waves have previously been studied by Mougel *et al.* (2015, 2017) in a confined geometry for background flows with particular forms, such as solid-body rotation or a potential vortex flow. These studies neglect surface tension, which, for water and wavelengths longer than the order of millimeters, is justified; we will also neglect surface tension in what follows. Their studies reveal the presence of four main types of waves: surface gravity waves, inertial waves, Rossby waves, and centrifugal waves. The first three waves are observed for solid-body rotation, while centrifugal waves and gravity waves arise with the potential vortex flow. Depending on the problem, each of these waves can be easily recognized and distinguished by its spatial structure and the associated frequency of oscillation. Further examples of problems where surface gravity waves,

inertial waves and Rossby waves appear can be found in Johnson (1997), Greenspan (1969) and McWilliams (2006), respectively. An interesting feature of the study on the potential vortex flow is the possibility of an instability of the base solution due to an interaction between the centrifugal and gravity waves. This interaction mechanism was initially studied by Mougel *et al.* (2014) for a Rankine-vortex (made up of an inner solid-body rotation and an outer potential vortex), although the origins and nature of this instability do not appear to have been fully investigated. Surface waves have been also studied by Hunt *et al.* (2015), particularly considering the effects of an electric field on both linear and nonlinear inviscid, irrotational waves. Moreover, two-dimensional surface waves in electrohydrodynamics and magneohydrodynamics have been studied by Hunt & Vanden-Broeck (2015); Hunt (2019); Hunt & Dutykh (2021), although in the present work we do not take into account any electric or magnetic field, but instead we consider the full three-dimensional linear response to a prescribed swirling flow.

The work in this paper considers a laterally unbounded domain (i.e. a domain of infinite radial extent) with a finite depth, assuming neither a shallow water nor a deep water limit. The problem of studying waves scattered by a vortex flow in a horizontally unbounded domain in a two-dimensional shallow-water setting with a bathtub vortex as a background flow was considered by Patrick *et al.* (2018) and Patrick (2019), in order to provide an analogy between fluid phenomena and black holes. Their study revealed the presence of what they called “quasibound states”: normal modes having a very slow decaying rate in time and a spatial structure which remains trapped within the vortex core region; this is perhaps understandable, since their bathtub vortex includes an inflow towards the vortex. In our work we investigate whether this result can be generalized to purely rotating flows in non-shallow water where the axial variation of the perturbations cannot be neglected anymore.

In order to numerically study wave propagation problems in an unbounded domain, a Non-Reflecting Boundary Condition (NRBC) needs to be imposed at infinity. This is relatively straightforward in a two-dimensional shallow-water setting, since the dispersion relation for surface waves is known, and hence a characteristics analysis (Fritz 1978) allows the imposition of an exact NRBC. Characteristic boundary conditions are, however, specific to classical hyperbolic wave equations (Grote & Keller 1995; Grote 2000; Keller & Givoli 1989; Bayliss & Turkel 1980; Engquist & Majda 1977). Such exact boundary conditions cannot be directly imposed on our three-dimensional problem, as our problem is not necessarily hyperbolic, and it is not possible to find real characteristics. Moreover, surface waves on non-shallow water are dispersive, with the propagation speed of each mode depending on its frequency, which significantly complicates a NRBC even for hyperbolic problems (e.g. Lindquist *et al.* 2012), and can limit the range of wavenumbers being correctly treated (e.g. Wellens & Borsboom 2019). One possible solution to this problem is provided by absorbing layer methods. The idea behind this class of techniques is to surround the actual computational domain by layers through which waves are progressively damped out until they reach the edge of the computational domain, where their amplitude is so small that any reflections will be negligible. The absorbing layers need to be introduced gradually, however, as otherwise waves can spuriously reflect from the edges of the absorbing layers. Absorbing layer methods have been applied initially to waves problems in electromagnetics (e.g. Berenger 1994) and then extended to other physical fields like elasticity and fluid dynamics. A shortcoming of absorbing layer formulations lies in the number of new unknowns introduced in the problem; this may be reduced using the formulation of Sim (2010) in the case of second order hyperbolic equations. Here, a related but different technique is developed for the absorbing layer

formulation in the far field, without introducing further unknowns in the mathematical problem.

The paper is organised as follows: in section 2, a general description is given of the mathematical model used to study perturbations to a Lamb–Oseen swirling flow, including a mathematical description of NRBCs. The resulting eigenvalue problem is then solved using a numerical procedure described in section 3. The results of this numerical solution are described in section 4. Finally, resulting conclusions and possible future directions for continued research are highlighted in section 5.

## 2. Mathematical Model

Assuming that viscosity is negligible over the timescales of interest here, the governing equations are the incompressible Euler equations,

$$\frac{\partial \mathbf{U}}{\partial t} + \mathbf{U} \cdot \nabla \mathbf{U} + \frac{1}{\rho} \nabla P + g \hat{\mathbf{z}} = 0, \quad \nabla \cdot \mathbf{U} = 0, \quad (2.1)$$

where  $\mathbf{U}$  is the fluid velocity,  $P$  is the fluid pressure,  $\hat{\mathbf{z}}$  is a unit vector in the vertical direction, and the constants  $\rho$  and  $g$  are the fluid density and the acceleration due to gravity respectively. The fluid is contained between a bottom boundary at  $z = 0$  and an upper free surface at  $z = H$ . The fluid must satisfy no penetration through the bottom boundary, giving  $\mathbf{U} \cdot \hat{\mathbf{z}} = 0$  at  $z = 0$ . Two boundary conditions, a kinematic and a dynamic boundary condition, must be satisfied along the free surface itself. Here, we assume the fluid above the free surface to be dynamically passive, and in particular, to have a constant pressure  $\bar{P}$ . Together, these give the boundary conditions

$$\frac{\partial H}{\partial t} + \mathbf{U} \cdot \nabla H = \mathbf{U} \cdot \hat{\mathbf{z}} \quad \text{and} \quad P = \bar{P} \quad \text{on} \quad z = H. \quad (2.2)$$

We split the overall velocity and pressure into a steady purely swirling base flow and a small (magnitude  $\varepsilon$ ) time-dependent perturbation, where

$$\mathbf{U} = U_0(r) \hat{\boldsymbol{\theta}} + \varepsilon(u_r \hat{\mathbf{r}} + u_\theta \hat{\boldsymbol{\theta}} + u_z \hat{\mathbf{z}}), \quad P = P_0(r, z) + \varepsilon p, \quad H = h_0(r) + \varepsilon h. \quad (2.3)$$

### 2.1. The steady base flow solution

A purely swirling steady base flow has a velocity given by  $\mathbf{U}_0 = U_0(r) \hat{\boldsymbol{\theta}}$ . The governing equations and boundary conditions for this steady flow are satisfied provided we take

$$P_0(r, z) = \bar{P} + \rho g (h_0(r) - z), \quad (2.4a)$$

$$h_0(r) = h_\infty - \frac{1}{g} \int_r^\infty \frac{U_0^2(r')}{r'} dr', \quad (2.4b)$$

where  $h_\infty$  is the depth of the fluid at  $r = \infty$ . This for any velocity profile  $U_0(r)$ . For the specific case of the Lamb–Oseen vortex considered here, we have

$$U_0(r) = \frac{\Gamma_0}{2\pi r} \left( 1 - \exp(-r^2/a^2) \right), \quad (2.5)$$

where  $a$  sets the radial size of the core and  $\Gamma_0$  sets the circulation of the vortex. Note that, for the Lamb–Oseen vortex, for small  $r$ , we have  $U_0(r) \approx r\Gamma_0/2\pi a^2$ , so that (2.5) is a solid body rotation near the centre of the vortex, while for large  $r$  we have  $U_0(r) \approx \Gamma_0/2\pi r$ , so that (2.5) is a potential swirl far from the centre of the vortex. A typical steady base flow free surface for the Lamb–Oseen vortex is shown in figure 2.

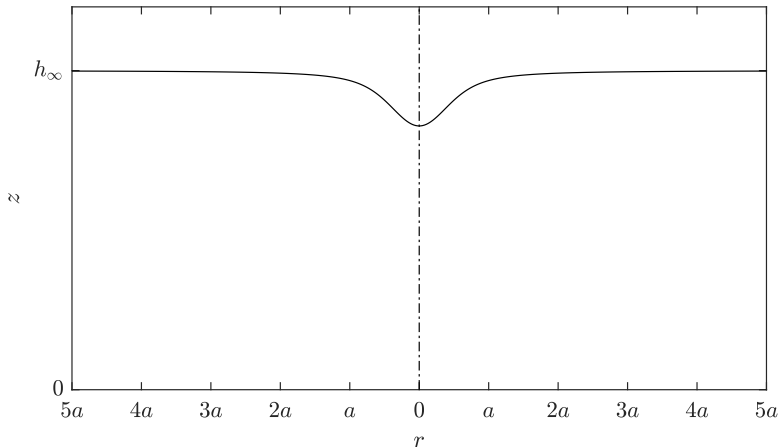


FIGURE 2. A typical section through a Lamb–Oseen vortex, showing the steady base flow free surface.

## 2.2. Perturbation Dynamics

Waves arise when a small perturbation is introduced to the steady base solution. By linearizing the governing equations (2.1) about the base solution  $(U_0, P_0, h_0)$  given above, the governing equations for the perturbation are

$$D_t u_r - 2\Omega_0(r)u_\theta + \frac{1}{\rho} \frac{\partial p}{\partial r} = 0, \quad (2.6a)$$

$$D_t u_\theta + \frac{1}{r} (rU_0(r))' u_r + \frac{1}{\rho r} \frac{\partial p}{\partial \theta} = 0, \quad (2.6b)$$

$$D_t u_z + \frac{1}{\rho} \frac{\partial p}{\partial z} = 0, \quad (2.6c)$$

$$\frac{1}{r} \frac{\partial}{\partial r} (r u_r) + \frac{1}{r} \frac{\partial u_\theta}{\partial \theta} + \frac{\partial u_z}{\partial z} = 0, \quad (2.6d)$$

where  $D_t = \partial_t + \Omega_0(r)\partial_\theta$  is the convective derivative and  $\Omega_0(r) = U_0(r)/r$  is the steady base flow angular velocity. (Here and throughout, primes denotes derivatives with respect to the argument for a function of only one variable). Linearizing the boundary conditions (2.2) about the steady base flow leads to

$$u_z = \frac{1}{\rho g} D_t p + h'_0 u_r \quad \text{and} \quad h = \frac{p}{\rho g} \quad \text{on} \quad z = h_0(r), \quad (2.7a)$$

$$u_z = 0 \quad \text{on} \quad z = 0. \quad (2.7b)$$

In addition to these boundary conditions, there is another implicit boundary condition, which is that there are no waves entering the domain from  $r = \infty$ , and thus only outgoing waves are allowed at  $r = \infty$ . This rather subtle boundary condition will become more concrete when we truncate the domain to finite  $r$  in order to numerically solve the above equations.

Before we progress further, we now make two changes to the governing equations for the perturbation. Firstly, since the governing equations for the perturbation are linear,

we may assume a modal solution of the form

$$\mathbf{u} = \left[ u(r, z)\hat{\mathbf{r}} + v(r, z)\hat{\boldsymbol{\theta}} + w(r, z)\hat{\mathbf{z}} \right] \exp(-i\omega t + im\theta), \quad (2.8a)$$

$$p = \phi(r, z) \exp(-i\omega t + im\theta), \quad (2.8b)$$

where  $m$  is restricted to integer values, since the solution must be  $2\pi$  periodic, while  $\omega$  in general will be complex, with  $\text{Re}(\omega)/2\pi$  being the oscillation frequency and  $-\text{Im}(\omega)$  being the decay rate. The eigenvalue problem that will eventually result will have  $\omega$  as the eigenvalue to be found.

Secondly, we re-write the governing equations and boundary conditions in a non-dimensional form. To do so, we choose the reference lengthscale to be  $a$ , the scale of the vortex core (equation (1) and figure 2). The reference time scale is that given by this lengthscale and gravity:  $\sqrt{a/g}$ . The velocity scale is thus  $\sqrt{ag}$ . All dimensional variable may then be expressed in terms of a nondimensional variable (denoted by a tilde), as

$$\begin{aligned} (r, \theta, z) &= (a\tilde{r}, \tilde{\theta}, a\tilde{z}), & t &= \sqrt{\frac{a}{g}}\tilde{t}, & U_0(r) &= \frac{\Gamma_0}{2\pi a}\tilde{U}_0(\tilde{r}), & \Omega_0 &= \frac{\Gamma_0}{2\pi a^2}\tilde{\Omega}_0, \\ h &= a\tilde{h}, & p &= \rho a g \tilde{p}, & \omega &= \sqrt{\frac{g}{a}}\tilde{\omega}, & \mathbf{u} &= \sqrt{ag}\tilde{\mathbf{u}}. \end{aligned} \quad (2.9)$$

There are two physical parameters that are not scaled to unity by this nondimensionalization: these may be thought of as the strength of the vortex and the depth of the fluid at infinity, given respectively as

$$F = \frac{\Gamma_0}{2\pi\sqrt{ga^3}}, \quad \tilde{h}_\infty = \frac{h_\infty}{a}. \quad (2.10)$$

$F$  is the Froude number and sets the nondimensionalized velocity of the vortex. Hence,  $F \rightarrow 0$  corresponds to a slow vortex with negligible steady surface height variation, while  $F \rightarrow \infty$  corresponds to a fast vortex with significant steady surface height variation, as can be seen from (2.13c) below. The dimensionless depth  $\tilde{h}_\infty$  is exactly that, so that the limit  $\tilde{h}_\infty \rightarrow 0$  corresponds to the shallow-water limit and  $\tilde{h}_\infty \rightarrow \infty$  corresponds to the deep-water limit. Care is needed, however, in considering the shallow-water limit: in what follows, we will assume that the steady fluid height never reaches zero, so that the bottom stays wetted, and consequently the shallow water limit  $\tilde{h}_\infty \rightarrow 0$  must be taken together with the slow wide vortex limit  $F \rightarrow 0$  such that  $\tilde{h}_\infty/F^2$  is bounded away from zero, as can also be seen from (2.13) below. The azimuthal wavenumber  $m$  is also a dimensionless parameter, and represents the rotational symmetry of the solution being investigated.

Dropping the tildes, the complete nondimensional eigenvalue problem is

$$(-i\omega + imF\Omega_0(r))u - 2F\Omega_0(r)v + \frac{\partial\phi}{\partial r} = 0, \quad (2.11a)$$

$$(-i\omega + imF\Omega_0(r))v + \frac{F}{r}(rU_0(r))'u + \frac{im}{r}\phi = 0, \quad (2.11b)$$

$$(-i\omega + imF\Omega_0(r))w + \frac{\partial\phi}{\partial z} = 0, \quad (2.11c)$$

$$\frac{1}{r}\frac{\partial}{\partial r}(ru) + \frac{im}{r}v + \frac{\partial w}{\partial z} = 0, \quad (2.11d)$$

together with the boundary conditions of no incoming modes at  $r = \infty$ , and

$$w = 0, \quad \text{on } z = 0, \quad (2.12a)$$

$$w = (-i\omega + imF\Omega_0(r))\phi + F^2r\Omega_0^2(r)u, \quad \text{on } z = h_0(r). \quad (2.12b)$$

For the Lamb–Oseen vortex, in dimensionless terms

$$U_0(r) = \frac{1 - \exp(-r^2)}{r}, \quad \Omega_0(r) = \frac{U_0(r)}{r}, \quad h_0(r) = h_\infty - F^2 \int_r^\infty \frac{U_0^2(r')}{r'} dr'. \quad (2.13a, b, c)$$

### 3. Numerical methods

#### 3.1. Absorbing layer for 3D incompressible Euler equations

In practice, we solve the eigenvalue problem in a finite computational domain and hence introduce an artificial boundary at finite radius  $R$ . The far-field boundary condition of no incoming waves becomes a non-reflecting boundary condition (NRBC) at this boundary. However, exact NRBCs are generally derived using the method of characteristics, but this is not available to us since (2.11d) is not hyperbolic. A widely used alternative is based on damping layers or even perfectly matched layers. The idea is to introduce a “damping layer” — also called an “absorbing layer” — surrounding the computational outer boundary. In the damping layer, waves are progressively damped until their amplitude is sufficiently small that reflections from the outer boundary do not reenter the main computational domain. Outgoing waves are effectively absorbed in the layer. The boundary condition at the outer boundary of the computational domain is then unimportant, and is typically taken to be either a Dirichlet-type or Neumann-type boundary condition. To add damping to our governing equations, we add a “damped compressibility” term into the continuity equation (2.11d) of the form  $\xi(r)\phi$ , where  $\xi(r)$  is a sufficiently smooth function that is identically zero outside the damping region. We then impose a Dirichlet boundary condition on the pressure at an artificial boundary  $r = R \gg 1$ . Equation (2.11d) then becomes

$$\xi(r)\phi + \frac{1}{r} \frac{\partial}{\partial r} (ru) + \frac{im}{r} v + \frac{\partial w}{\partial z} = 0. \quad (3.1)$$

Here, we choose a simple form for  $\xi(r)$ , which we will demonstrate works well for the parameters we consider here:

$$\xi(r) = \begin{cases} 0, & r < R_c, \\ \bar{\xi} \left( \frac{r - R_c}{R - R_c} \right)^2, & R_c \leq r \leq R. \end{cases} \quad (3.2)$$

This gives a damping region  $r \in [R_c, R]$  with a strength governed by the constant  $\bar{\xi}$ . The governing equations (2.11a–c) together with the modified continuity equation (3.1) and boundary conditions (2.12) form an eigenvalue problem to solve for the allowable frequencies  $\omega$  permitting a nonzero modal solution.

#### 3.2. Numerical discretization

In order to solve (2.11a–c, 2.12, 3.1), we used a Galerkin spectral method and expand with a combination of Legendre polynomials as basis functions in both the radial and axial coordinate in order to satisfy the Dirichlet boundary conditions. We also remap the domain from the physical domain  $D = [0, R] \times [0, h_0(r)]$  to the computational square

domain  $S = [-1, 1] \times [-1, 1]$  to account for the shape of the computational domain with a variable surface height  $h_0(r)$ . We then obtain the weak formulation of the problem. Full details are given in appendix A. The discretized version ends up being of the form

$$\mathbf{A}\mathbf{w} = \omega\mathbf{B}\mathbf{w}, \quad (3.3)$$

with  $\mathbf{w} = (u_{ij}, v_{ij}, w_{ij}, \phi_{ij})$  representing our array containing the spectral coefficients of each unknown,  $\mathbf{A}$  and  $\mathbf{B}$  being matrices of order  $4N_xN_y \times 4N_xN_y$ , where  $N_x$  and  $N_y$  are the number of Legendre polynomials used in the radial and vertical directions respectively. This discretized problem may then be solved using any numerical eigenvalue solver; here, we use the `eig` solver in MATLAB.

Not all solutions to the discretized problem (3.3) correspond to solutions to the continuous problem being approximated, however. To remove under-resolved eigenmodes and spurious eigenvalues, the numerical solutions to (3.3) are filtered, as described in the appendix (A.2).

### 3.3. Spurious reflected modes

The finite numerical domain and damping region introduces another source of spurious modes besides those coming from the numerical discretization, namely those modes which are well-resolved but which include a significant reflection from either the damping boundary at  $r = R_c$  or the truncation boundary at  $r = R$ . Such spurious eigenmodes are affected by the values of  $R_c$  and  $R$ , and by the amount of damping  $\bar{\xi}$ , whereas good approximations to the modes on the infinite domain should be insensitive to these values. Since  $-\text{Im}(\omega)$  is the decay rate of the mode, variations in damping typically have a strong effect on  $\text{Im}(\omega)$  for spurious reflected modes. We may therefore remove these spurious reflected modes by running our numerical code twice: the first time with a suitably chosen amount of damping  $\bar{\xi}$ , and the second time with twice that amount of damping  $2\bar{\xi}$ . Only those modes whose eigenvalues do not change significantly with the change in the damping coefficient are retained (as measured using the same metric (A 11) used for the numerical resolution).

### 3.4. Numerical convergence study

The first convergence study involves varying the amount of damping in the damping layer and checking that the eigenvalues do not change, nor does the shape of the corresponding eigenfunctions in the physical domain  $r < R_c$ . Here we present the convergence results for  $m = 7$  and  $F = 0.3$ , as these parameters support a radiating mode which is the most stringent test of a non-reflecting boundary condition. For varying magnitudes of damping  $\bar{\xi}$ , the radiating eigenfunction is plotted in figure 3, and the corresponding eigenvalues are given in table 1. The damping clearly influences the eigenfunction shape, and for  $\bar{\xi} \in \{0.01, 0.1\}$  a clear standing wave shape is seen. For  $\bar{\xi} \in \{1, 5, 10\}$ , the eigenfunctions are practically identical in the physical domain  $0 < r < R_c$ , and only differ in the damping layer  $R_c \leq r \leq R$ . For  $\bar{\xi} = 50$ , however, the damping is too strong, and little oscillations can be seen for  $r < R_c$ , suggesting wave reflection by the edge of the damping layer. This is also supported by the eigenvalues in table 1, which show the sensitivity of  $\text{Im}(\omega)$  to variations in damping strength, as expected.

The second convergence study involves varying the width of the damping layer whilst maintaining the same size of the computational domain  $R = 30$  and a fixed damping strength  $\bar{\xi} = 5$ . The eigenfunctions are displayed in figure 4, and the corresponding eigenvalues in table 2. For  $R_c = 15$  and  $R_c = 20$  the eigenfunctions can be seen to be



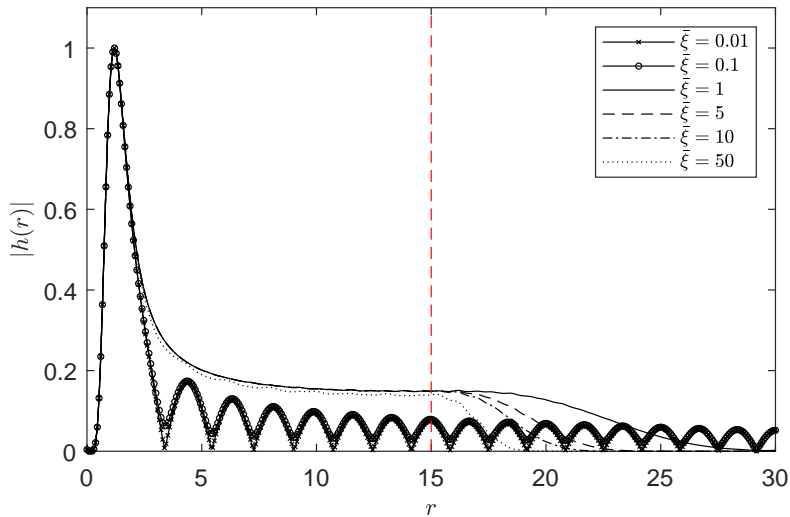


FIGURE 3. Eigenfunctions for  $m = 7$ ,  $F = 0.3$ ,  $R_c = 15$ ,  $R = 30$  and different values of  $\bar{\xi}$ . A vertical red-dashed line indicates the radial point  $R_c$  where the damping effect begins.

---

$\bar{\xi}$	0.01	0.1	1	5	10	50
$\text{Re}(\omega)$	-1.3774	-1.3774	-1.3773	-1.3773	-1.3773	-1.3777
$\text{Im}(\omega)$	-0.003	-0.0031	-0.0132	-0.0132	-0.0132	-0.0125

---

TABLE 1. Eigenvalues as function of the amount of damping for  $m = 7$  and  $F = 0.3$ ,  $R_c = 15$  and  $R = 30$ .

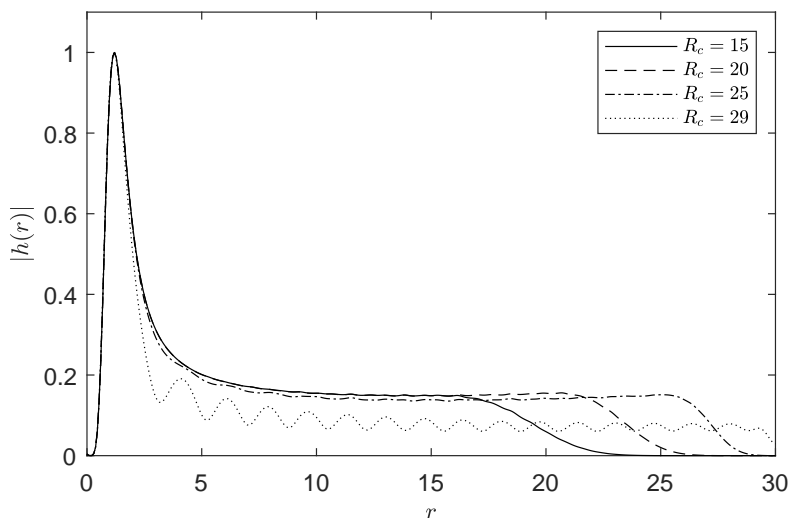


FIGURE 4. Eigenfunctions for  $m = 7$ ,  $F = 0.3$ ,  $\bar{\xi} = 5$ ,  $R = 30$  and different values of  $R_c$ .

---

$R_c$	15	20	25	29
$\text{Re}(\omega)$	-1.3773	-1.3773	-1.3775	-1.3807
$\text{Im}(\omega)$	-0.0132	-0.0132	-0.0124	-0.0065

---

TABLE 2. Eigenvalues as function of the initial position of the absorbing layer for  $m = 7$  and  $F = 0.3$ ,  $\bar{\xi} = 5$  and  $R = 30$ .

---

practically identical in the physical domain  $0 < r < R_c$ , while for  $R_c = 29$  a standing wave pattern can be seen, implying significant wave reflection from the truncation boundary at  $R = 30$ . Again, this is also seen for the variations in the eigenvalue, with again  $\text{Im}(\omega)$  being particularly sensitive.

### 3.5. Choice of numerical parameters

Based on numerical convergence studies such as those described above, for the results that follow we take  $R = 10$  and  $R_c = 5$ , with  $\bar{\xi} = 5$  (to which results are compared to  $\bar{\xi} = 10$ ). This choice is motivated by the need for sufficiently high resolution to resolve all modes of interest in the range of Froude numbers and azimuthal wavenumbers considered. The eigenvalue tolerance and eigenfunction resolvedness tolerance are taken to be  $\text{tol} = 10^{-2}$  and  $10^{-1}$  respectively, whereas other numerical parameters are taken to be  $N_x = 50$ ,  $N_y = 20$ ,  $b_x = 12$  and  $b_y = 4$ , as explained in more details in appendix A. For all results presented here, we use a fluid depth of  $h_\infty = 5$ . This is the depth shown in figure 2. This value is large enough to allow for a wide range of Froude numbers ( $0 \leq F < \sqrt{\frac{h_\infty}{\log(2)}} \simeq 2.68$ ) without forming a dry region near  $r = 0$ , while small enough to exhibit finite-depth effects.

## 4. Results

Here, we compute leading (i.e. least damped) eigenmodes for a range of azimuthal wave numbers as large as  $m = 20$  and find that above  $m = 6$  surface pressure waves dominate. We shall first present the surface waves for a representative case, wavenumber  $m = 7$ , and discuss in detail how the modes and eigenvalues depend on Froude number for this case. Following this, we consider the dependence of modes and eigenvalues on the azimuthal wave number.

### 4.1. Representative case $m = 7$

We begin with a detailed description of the case azimuthal wavenumber  $m = 7$ . The reason for taking such value of  $m$  is dictated both by the explanatory picture in Patrick *et al.* (2018, pp.6), who show a picture of the spiral structure of a normal mode solution for sufficiently high azimuthal wavenumber, as well as by the reasonable amount of computational time needed to get the leading surface waves eigenmodes. Indeed, we find numerically that the spatial structure of surface gravity waves becomes thinner and more localized close to the free surface as  $m$  increases. Following particularly the latest argument, the case of  $m = 7$  has been taken as a reference study case and in the following we are going to show most of the interesting features applied to this case.

One of the key results of our study is the change in character of modes as function the

rotation rate of the vortex. Specifically, we distinguish two classes of modes: radiating modes and trapped modes. The spatial structure of the radiating modes has a characteristic spiral shape, as shown in figure 5a, and a long tail in the radial direction, as shown in figure 6a. Such modes behave as travelling waves along the radial direction and are responsible for the dissipation of the initial energy put into the system to excite the mode. In contrast, trapped modes are confined to a bounded region in the radial direction, and without the spiraling structure seen for the radiating modes. Those modes behave as standing waves along the radial direction and are non-dissipative. Examples can be seen in figures 5e and 6e. The distinction between radiating and trapped modes can further be seen in the eigenvalues. Indeed, radiating modes have eigenvalues with a negative imaginary part, indicating exponential decay in time, whereas trapped modes have a negligible imaginary part and so do not appreciably decay in time.

Figures 5 and 6 show representative examples of the continuous, but rapid, transition from radiating modes to trapped modes as the Froude number (the dimensionless rotation rate of the vortex), increases. This transition between radiating and trapped modes is also seen in figure 7 where the modulus of the free surface height is plotted as a function of  $r$  for different Froude numbers.

To look more closely at the trend in the eigensolutions, let us first denote by  $n$  an integer representing the number of peaks in radial direction of the modulus of the pressure eigenfunctions, as displayed in figure 8. In this way each eigensolution will be indexed by both  $m$  and  $n$ , with corresponding eigenvalues  $\omega = \omega_{mn}$ . In figure 9a, the two types of modes can be seen: radiating modes with a significant negative  $\text{Im}(\omega)$ , and trapped modes having an almost null  $\text{Im}(\omega)$ . There is no sharp transition between radiating and trapped modes. Accordingly, here we set an arbitrary threshold to separate the two sets of modes by considering a mode to be trapped when its eigenvalue has an imaginary part smaller than  $10^{-5}$  in modulus (although our results are relatively insensitive to this threshold; see figure 12). Hence, while the trapped modes considered here are almost neutrally stable, they have eigenvalues with small negative imaginary part and even almost entirely trapped modes radiate very slightly. Interestingly, none of the modes computed here are observed to become linearly unstable, and we hypothesise that the base solution is at most marginally stable, but not unstable, to linear perturbations of this type at large Froude number. We note that our numerical results show a third region in this diagram below a finite threshold value of the Froude number where no normal modes seems to exist. Indeed, in our calculations the eigenmodes for sufficiently low Froude numbers become dependant on the amount of damping introduced in the system, and are therefore discarded. We leave to future studies the possibility of determining whether surface modes exist at low Froude numbers, although we can say based on our results that any such modes would necessarily be radiating rather than trapped.

Another interesting phenomenon concerns the spinning direction of waves with respect to the vortex flow as the rotation rate is varied. This is shown in figure 9b, which shows how the real part of the eigenvalues varies with the Froude number, again for  $m = 7$ . For  $\text{Re}(\omega) < 0$ , waves spin opposite to the base flow (counter-rotating waves), while for  $\text{Re}(\omega) > 0$ , waves rotate in the same direction with the flow (co-rotating waves). It is clear that for each  $n$ , there is a value of Froude number separating counter-rotating from co-rotating surface waves.

#### 4.2. Extension to higher azimuthal wavenumbers.

The results described above for  $m = 7$  are found to be typical at larger azimuthal wavenumbers. Figure 10 shows the trend of the imaginary part of the eigenvalues as a function of the Froude number. The results are qualitatively similar to the  $m = 7$  case.

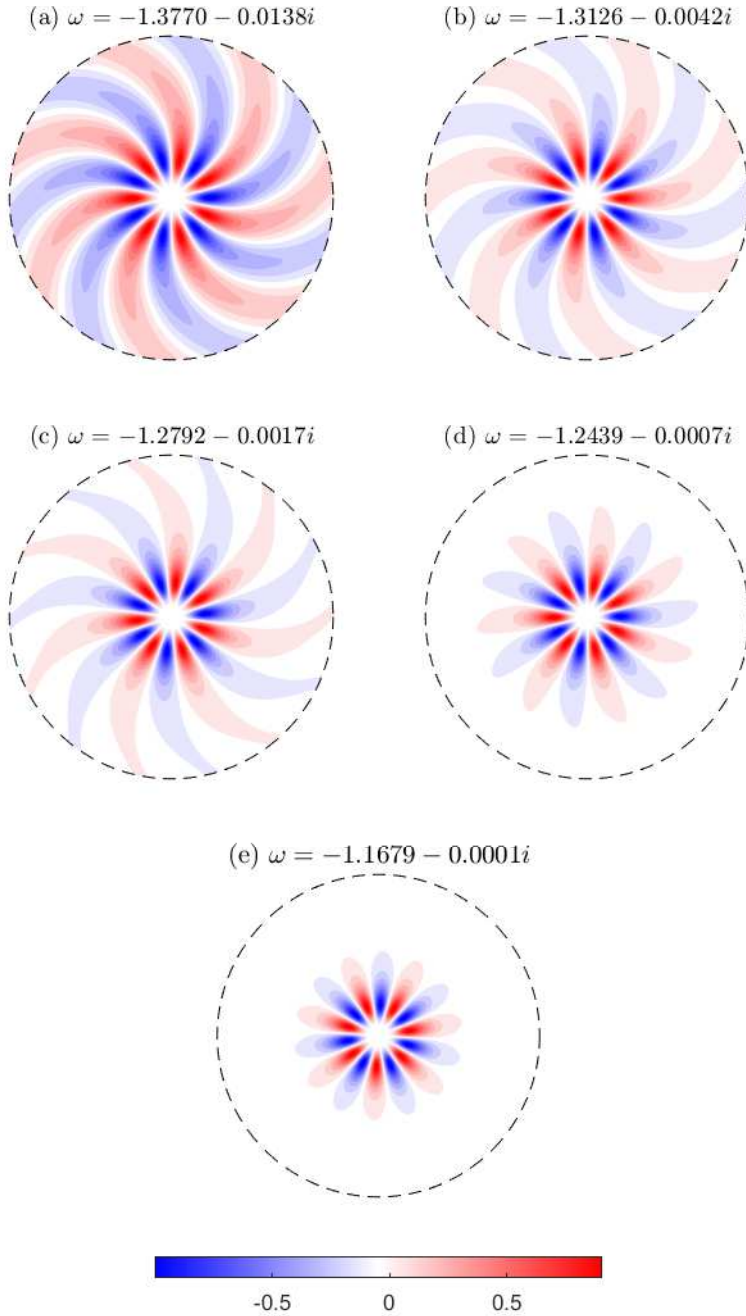


FIGURE 5. Plots of the free surface height  $h(r, \theta, t = 0) = \text{Re}[\phi(r, h_0(r)) \exp\{im\theta\}]$  for  $m = 7$ . (a)  $F = 0.3$ . (b)  $F = 0.32$ . (c)  $F = 0.33$ . (d)  $F = 0.34$ . (e)  $F = 0.36$ . All modes displayed rotate clockwise, i.e. against the vortex flow.

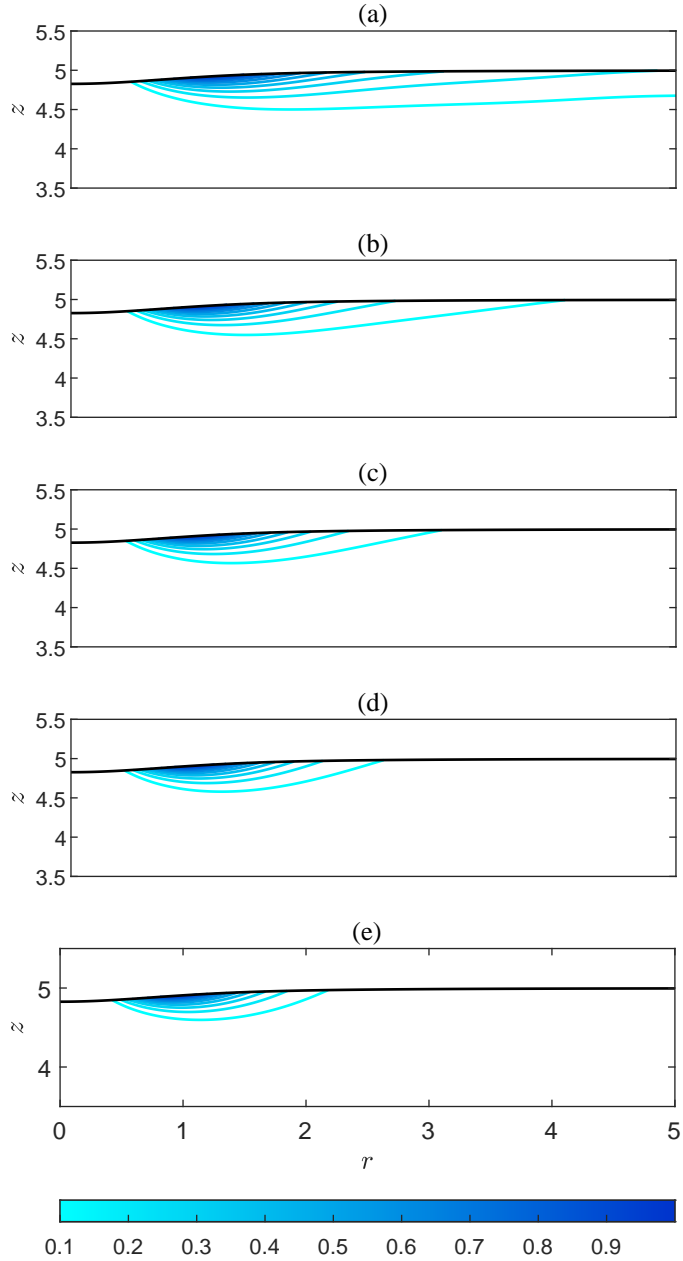


FIGURE 6. Plots of the pressure distribution  $|\phi_m(r, z)|$  for  $m = 7$ . (a)  $F = 0.3$ . (b)  $F = 0.32$ . (c)  $F = 0.33$ . (d)  $F = 0.34$ . (e)  $F = 0.36$ .

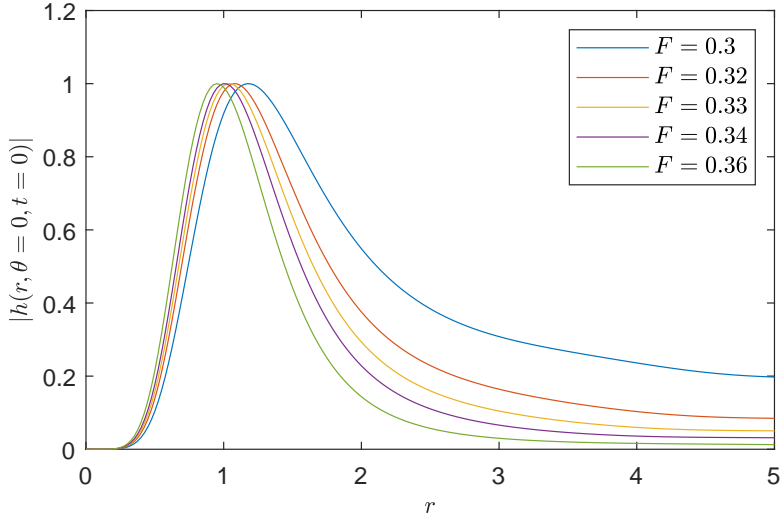


FIGURE 7. Modulus of the free surface height along the radius for  $m = 7$  in the transition regime from radiating to trapped modes.

Eigenvalue branches shift to lower  $F$  with increasing  $m$ , thus shifting to lower  $F$  both the value of  $F$  separating radiating and trapped modes and the asymptotic value of  $F$  below which normal modes are not found by our methods. This suggests that for very high azimuthal wavenumber perturbations we expect to get radiating eigenmodes at lower and lower Froude numbers, as shown in figure 11 for the example cases of  $m = 15$  and  $m = 20$ .

We have computed the range of Froude numbers in which modes radiate and transition towards a neutrally stable state for different values of  $m$ . This is summarized in figure 12 showing the classes of solutions previously described, now in the whole range  $(m, F) \in [3, 20] \times [0, 1]$ . Also included in this figure is the dividing line between counter-rotating and co-rotating trapped modes. Two notable features of the plot are the shift of contours to larger  $F$  and the widening of the separation between contours with decreasing  $m$ . Both of these features are consistent with figure 10, where one sees not only a shift in the eigenvalue curves with  $m$ , but also a steepening of the transition between radiating and trapped modes with increasing  $m$ .

## 5. Conclusions and future developments

We have considered the linear response to small perturbations to a free surface Lamb–Oseen vortex flow in a laterally unbounded domain. We restricted our focus to surface waves, as it was these waves that were seen in the motivating experiments; we note that the numerical procedure described here also calculates other types of modes which we have not investigated further here. This is particularly true for inertial waves which turned out to be the least damped modes for perturbations having azimuthal modenumber  $m = 0, 1, 2$  over the range of Froude numbers considered ( $F \in [0, 1]$ ). Thus, we have not shown results for these three cases.

Our study revealed the presence of two classes of surface modes: radiating modes and trapped modes. While these have previously been seen for shallow water vortices with inflow (such as a plughole vortex), here we have shown that they arise in a fully

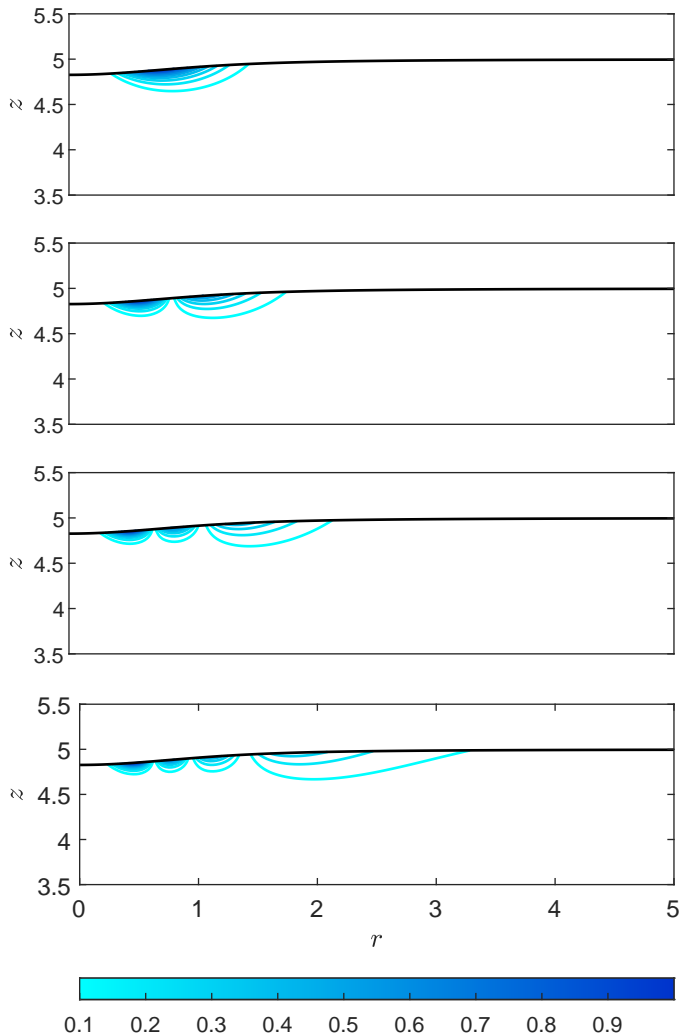


FIGURE 8. Modulus of the pressure  $|\phi_m(r, z)|$  for  $m = 7$  and  $F = 0.5$ . We show the four least stable eigenmodes for such parameters, having one, two, three and four peaks respectively.

3D non-shallow-water problem without the need for an inflow to help trap the modes. Our numerical predictions show the appearance of such modes above a threshold value of the rotation rate for a given azimuthal modal perturbation. In terms of features of the eigenmode solutions, radiating modes are dissipative, and have a spatial structure which extends in the horizontal plane, therefore behaving as radially-travelling waves. By contrast, trapped modes, by virtue of their zero growth rate, persist for long times without dissipating and remain localized within the core region of the vortex. Their spatio-temporal behaviour resembles that of a radially-standing wave instead of a radially-travelling wave. Our computations also suggest that trapped modes will asymptotically approach a neutrally stable state in the limit of large Froude number without becoming unstable, although the exact asymptotic scaling of  $\text{Im}(\omega)$  for large  $F$  was not obvious from the numerical analysis carried out here. Finally, we have confirmed what has been seen in the initial motivating experiment of the pool, namely that modes can spin in

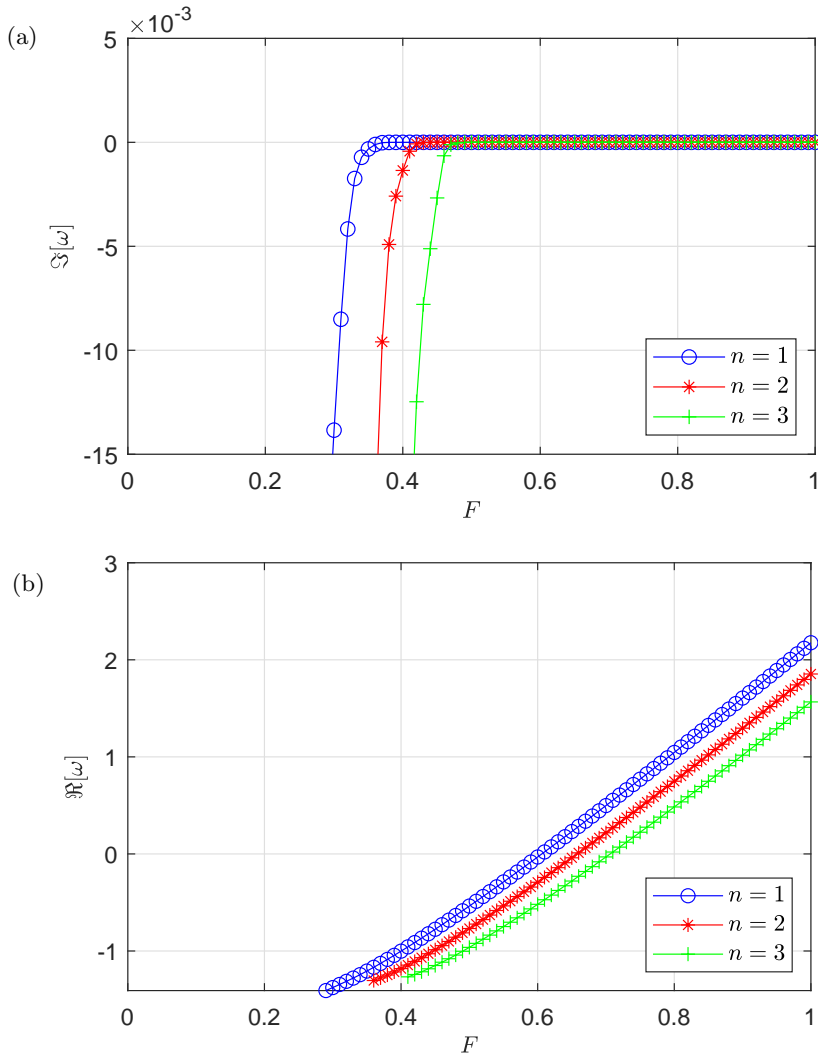


FIGURE 9. Imaginary (top) and real (bottom) parts of the eigenvalue  $\omega_{mn}$  as function of the Froude number  $F$  for  $m = 7$  and varying  $n$ .

either the same direction or the opposite direction to the base swirling flow. Such a trend varies with the rotation rate of the vortex, as summarised in figure 12.

To numerically simulate a (horizontally-)unbounded fluid on a bounded numerical domain, a far-field nonreflecting boundary condition or buffer region is needed. Here, a novel additional term is introduced into the governing equations, to provide damping of the surface waves in the buffer region only. While this method is less efficient than applying a non-reflecting boundary condition at the exact edge of the physical domain, it has proved more accurate than any non-reflecting boundary condition we implemented while remaining computationally viable. Indeed, introduction of additional unknowns in the mathematical formulation was not needed, thus overcoming the main drawback of PML methods. Furthermore, given that the background vortex flow vanishes in the far-field, the same absorbing layer formulation can be employed with other similar vortex distributions.



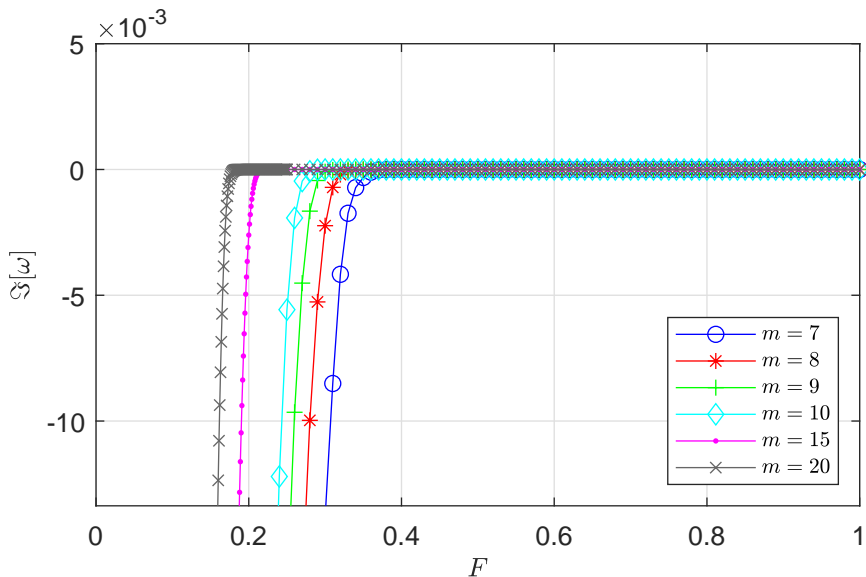


FIGURE 10. Imaginary part of the eigenvalues as functions of  $F$  for different values of  $m$ .

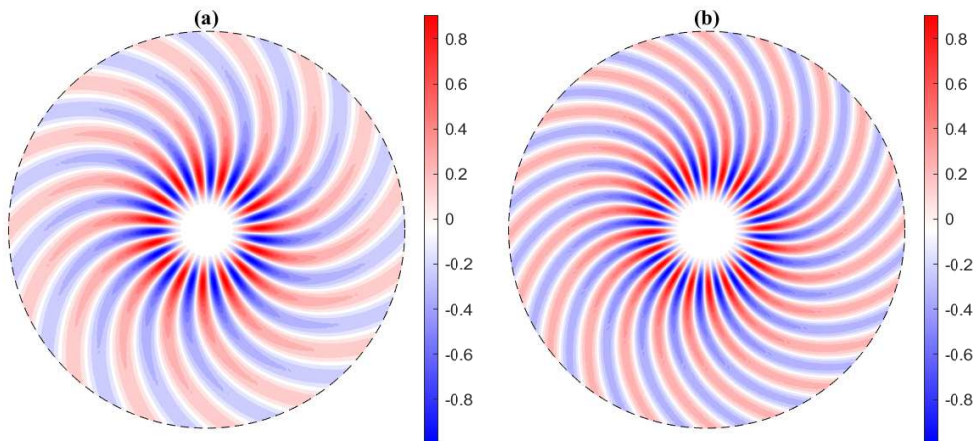


FIGURE 11. Shape of the free surface height  $h(r, \theta, t = 0) = \text{Re}[\phi(r, h_0(r)) \exp\{im\theta\}]$  in two high azimuthal wavenumber cases. (a):  $m = 15, F = 0.19$ . (b):  $m = 20, F = 0.16$ .

Due to the computational expense, we have left to future studies the extension of our parametric study of waves to extreme Froude numbers. In particular it would be interesting to investigate the trend of modes for very small and very large Froude numbers. Also, consideration of lower or higher aspect ratios  $h_\infty$  could be investigated. Our model also neglects both nonlinear and surface tension effects. While this is justified for the swimming pool application we model here, these assumptions break down at either large amplitudes or short wavelengths. Therefore, it would be interesting to investigate whether their inclusion could lead to an instability of the base vortex flow.

The numerical expense of our eigenvalue problem (which is a two-dimensional spatial

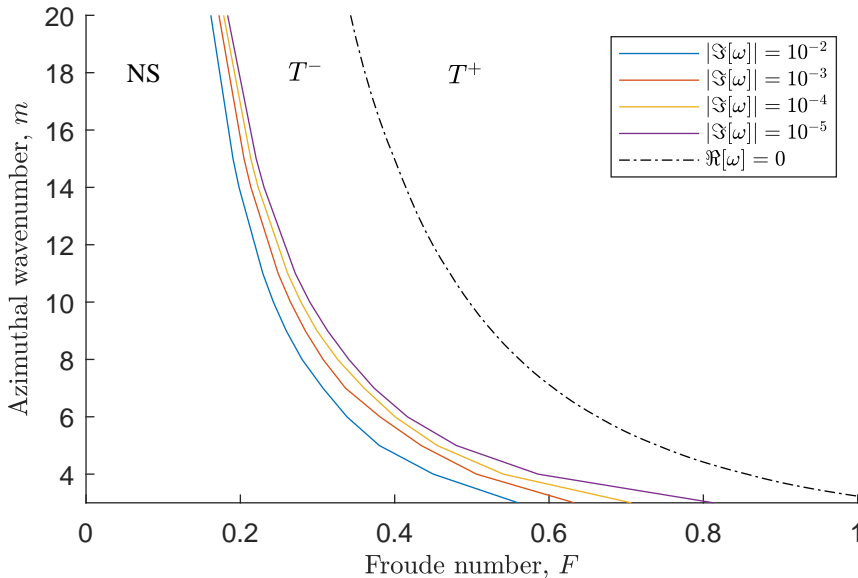


FIGURE 12. Regimes of radiating and trapped modes for different azimuthal wavenumbers  $m$  and Froude numbers  $F$ . Full coloured lines identify the radiating modes area with different radiation intensity.  $T^-$  identifies counter-rotating trapped modes,  $T^+$  co-rotating trapped modes. Dash-dotted line separates counter-rotating and co-rotating trapped modes. Finally NS identifies the region where normal mode solutions have not been found.

problem involving both  $r$  and  $z$  coordinates) might be reduced by investigating a one-dimensional approximation along the radial coordinate only; for example in either the deep- or shallow-water limits. Moreover, new methods and formulations for the imposition of a Non-Reflecting Boundary Condition in the far-field would certainly lead to a saving in the computational time as it will avoid—for example—the need to numerically resolve the unphysical buffer region.

**Acknowledgements.** E. Zuccoli was funded through the Warwick Mathematics Institute Centre for Doctoral Training, and gratefully acknowledges the support of the University of Warwick and the UK Engineering and Physical Sciences Research Council (EPSRC grant EP/W523793/1). E.J. Brambley gratefully acknowledges the support of the UK Engineering and Physical Sciences Research Council (EPSRC grant EP/V002929/1). D. Barkley gratefully acknowledges supported from the Simons Foundation (Grant No. 662985, NG). The authors are grateful to J.M. Skipp for the initial motivation and videos motivating this project.

**Declaration of Interests.** The authors report no conflict of interest.

## Appendix A. Detailed derivation and analysis of the Numerical Solution

### A.1. Numerical solution of the eigenvalue problem

In order to solve (2.11,2.12,3.1), we used a Galerkin Spectral Method and expand with a combination of Legendre polynomials as basis functions in both the radial and axial coordinate in order to satisfy the Dirichlet boundary conditions. First of all, to account for the shape of the computational domain with a variable surface height  $h_0(r)$ , we remap

the domain from the physical domain  $D = [0, R] \times [0, h_0(r)]$  to the computational square domain  $S = [-1, 1] \times [-1, 1]$  using the non-orthogonal transformation

$$x = \frac{2}{R}r - 1, \quad y = 2\frac{z}{h_0(r)} - 1. \quad (\text{A } 1)$$

In this new domain  $S$ , the problem becomes

$$imF\Omega_0(x)u - 2F\Omega_0(x)v + \frac{2}{R} \left[ \frac{\partial\phi}{\partial x} - \frac{h'_0(x)}{h_0(x)}(y+1) \frac{\partial\phi}{\partial y} \right] = i\omega u, \quad (\text{A } 2a)$$

$$imF\Omega_0(x)v + \frac{2F}{R(x+1)} \frac{d}{dx} [(x+1)U_0(x)]u + \frac{2im}{R(x+1)}\phi = i\omega v, \quad (\text{A } 2b)$$

$$imF\Omega_0(x)w + \frac{2}{h_0(x)} \frac{\partial\phi}{\partial y} = i\omega w, \quad (\text{A } 2c)$$

$$\begin{aligned} \frac{2}{R(x+1)} \frac{\partial}{\partial x} [(x+1)u] + \frac{2}{R} \frac{h'_0(x)}{h_0(x)}u + \frac{2im}{R(x+1)}v \\ + \frac{2}{h_0(x)} \frac{\partial}{\partial y} \left[ w - \frac{h'_0(x)}{R}(y+1)u \right] + \xi(x)\phi = 0, \end{aligned} \quad (\text{A } 2d)$$

$$imF\Omega_0(x)\phi(x, 1) + \frac{2h'_0(x)}{R}u(x, 1) - w(x, 1) = i\omega\phi(x, 1), \quad (\text{A } 2e)$$

$$w(x, -1) = 0, \quad \phi(1, y) = 0, \quad |\mathbf{u}(-1, y)| < \infty, \quad |\phi(-1, y)| < \infty. \quad (\text{A } 2f)$$

For  $R_c \leq r \leq R$ , we include a damping layer with a nonzero  $\xi(r)$ . Here, we choose a simple form for  $\xi(r)$ , which we demonstrate in section 3.4 works well for the parameters we consider here:

$$\xi(r) = \begin{cases} 0, & r < R_c, \\ \bar{\xi} \left( \frac{r - R_c}{R - R_c} \right)^2, & R_c \leq r \leq R. \end{cases} \quad (\text{A } 3)$$

Since  $\xi(r)$  is continuously differentiable at  $r = R_c$ , no special transmission conditions are needed there (Sim 2010, p. 46).

We next obtain the weak discretized formulation of this problem. The basis functions are chosen such that they identically satisfy the homogeneous Dirichlet boundary data. Also, the specific expansion of each variable in terms of basis functions will depend on the value of the azimuthal wavenumber, as this is associated with a singularity at the origin for the pressure and the aximuthal velocity component. In the following we make the distinction between the case of axisymmetric perturbations ( $m = 0$ ), and generic non-axisymmetric perturbations ( $m \neq 0$ ).

#### A.1.1. Discrete problem for non-axisymmetric perturbations

In the general case of a nonzero value of  $m$ , the weak formulation of the eigenvalue problem can be obtained in the following way. First of all, we notice the presence of singular terms at  $r = 0$  for  $u, v, \phi$  so we will require these function to be null at the origin. Consequently, even  $w$  will be so. Thus, we look at the unknowns in the following spaces:

$$[u, v, \phi] \in V_H(S) = \{(u, v, \phi) \in H^1(S) : (u, v, \phi) = 0, \quad \text{at } r = 0\}, \quad (\text{A } 4a)$$

$$w \in V_v(S) = \{w \in H^1(S) : w = 0, \quad \text{at } r = 0, \quad z = 0\}, \quad (\text{A } 4b)$$

where  $H^1(S)$  is the usual Sobolev space (Quarteroni 2009, ch. 2). We multiply the azimuthal component of the momentum equation and the continuity equation by  $(x+1)$ . Then, by multiplying each of the equations by suitable test functions  $(v_x, v_t, v_y, q)$  in the same space as the corresponding unknowns, after integrating over the square  $S$  and exploiting the boundary conditions, the weak formulation of the differential problem reads: find  $([u, v, \phi], w) \in V_H(S) \times V_v(S)$  such that  $\forall ([v_x, v_t, q], v_v) \in V_H(S) \times V_v(S)$  the following holds:

$$\int_S v_x \text{im} F \Omega_0(x) u - \int_S v_x 2F \Omega_0(x) v - \int_S \frac{2}{R} \frac{\partial v_x}{\partial x} \phi - \int_S v_x \frac{2}{R} \frac{h'_0(x)}{h_0(x)} (y+1) \frac{\partial \phi}{\partial y} = i\omega \int_S v_x u, \quad (\text{A } 5a)$$

$$\int_S v_t \left[ \text{im} F \Omega_0(x) (x+1) v + \frac{2F}{R} [(x+1) U_0(x)] u + \frac{2\text{im}}{R} \phi \right] = i\omega \int_S v_t (x+1) v, \quad (\text{A } 5b)$$

$$\int_S v_y \left[ \text{im} F \Omega_0(x) w + \frac{2}{h_0(x)} \frac{\partial \phi}{\partial y} \right] = i\omega \int_S v_y w, \quad (\text{A } 5c)$$

$$\begin{aligned} & \int_S \frac{2}{R} q \frac{\partial}{\partial x} [(x+1) u] + \int_S \frac{2}{R} \frac{h'_0(x)}{h_0(x)} (x+1) \left[ qu + \frac{\partial q}{\partial y} u \right] + \int_S \frac{2\text{im}}{R} qv \\ & - \int_S \frac{2}{h_0(x)} (x+1) \frac{\partial q}{\partial y} w + \int_{x=-1}^{x=1} \frac{2\text{im} F (x+1) \Omega_0(x)}{h_0(x)} q(x, 1) \phi(x, 1) \\ & = i\omega \int_{x=-1}^{x=1} \frac{2(x+1)}{h_0(x)} q(x, 1) \phi(x, 1). \end{aligned} \quad (\text{A } 5d)$$

Let us define the bilinear forms  $\mathcal{A} : V_H \times V_v \rightarrow \mathbb{R}$  and  $\mathcal{B} : V_H \times V_v \rightarrow \mathbb{R}$  such that the generalised eigenvalue problem above can be compactly written as: find  $([u, v, \phi], w) \in V_H \times V_v$  such that

$$\mathcal{A}([u, v, w, \phi], [v_x, v_t, v_y, q]) = \omega \mathcal{B}([u, v, w, \phi], [v_x, v_t, v_y, q]), \quad \forall ([v_x, v_t, q], u_y) \in V_H \times V_v \quad (\text{A } 6)$$

At this point, in order to discretize the problem, we need to expand the unknowns in terms of proper basis functions. Such basis functions are taken in such a way the homogeneous Dirichlet boundary conditions are automatically satisfied in both the axial and radial coordinates. In particular, we define the following set of polynomials,  $P_n^*(x)$  as follows:

$$P_n^*(x) = P_n(x) - P_{n-1}(x), \quad n \geq 1, \quad (\text{A } 7)$$

where  $P_n(x)$  are standard Legendre polynomials.

Thanks to the above definition, a Dirichlet boundary condition at  $x = 0$  is automatically satisfied. Therefore, we expand the velocity components and the pressure as

$$\begin{aligned} [u, v, \phi](x, y) &= \sum_{i=1}^{N_x} \sum_{j=1}^{N_y} [u_{ij}, v_{ij}, \phi_{ij}] P_i^*(x) P_j(y), \\ w(x, y) &= \sum_{i=1}^{N_x} \sum_{j=1}^{N_y} w_{ij} P_i^*(x) P_j^*(y). \end{aligned} \quad (\text{A } 8)$$

After substituting the expansion into the weak formulation (A 6), we obtain the final discrete eigenvalue problem, which reads

$$\mathbf{A} \mathbf{w} = \omega \mathbf{B} \mathbf{w}, \quad (\text{A } 9)$$

where  $\mathbf{w} = (u_{ij}, v_{ij}, w_{ij}, \phi_{ij})$  is our array containing the spectral coefficients previously

defined,  $\mathbf{A}$  and  $\mathbf{B}$  are the matrices of order  $4N_x N_y \times 4N_x N_y$  coming from the evaluation of the integrals appearing in the weak formulation for each equation.

### A.1.2. Discrete problem for axisymmetric perturbations

In the axisymmetric case ( $m = 0$ ), the differential problem (A 2) over the square  $S$  simplifies, and it can be noted that only the radial component of the velocity must go to zero as  $r \rightarrow 0$ , with the other unknowns allowed to take any finite value. Thus, studying the axisymmetric perturbation problem means to look for the eigensolutions in the following spaces:  $u \in V_H(S)$ ,  $(v, \phi) \in H^1(S)$  and  $w \in V_{v0} = \{w \in H^1(S) : w = 0, \text{ at } z = 0\}$ . The weak formulation is then obtained as shown previously. Regarding the discretization process, we express the four unknowns (and corresponding test functions) as follows

$$\begin{aligned} u(x, y) &= \sum_{i=1}^{N_x} \sum_{j=1}^{N_y} u_{ij} P_i^*(x) P_j(y), \\ [v, \phi](x, y) &= \sum_{i=1}^{N_x} \sum_{j=1}^{N_y} [v_{ij}, \phi_{ij}] P_i(x) P_j(y), \\ w(x, y) &= \sum_{i=1}^{N_x} \sum_{j=1}^{N_y} w_{ij} P_i(x) P_j^*(y). \end{aligned} \tag{A 10}$$

After substitution of the expansion above into the weak formulation, the resulting algebraic generalised eigenproblem (A 9) is recalled in the case  $m = 0$ .

### A.2. Spurious numerical modes and resolvedness conditions

Solving the discretized eigenvalue problem (A 9) is known to give rise to spurious eigenvalues and eigenfunctions. These are numerical artifacts caused by numerical under-resolution of highly-oscillatory modes; that is, eigenfunctions do satisfy the discretized problem but do not approximate solutions of the continuous eigenvalue problem. Following Brambley & Peake (2008) (see also Brambley 2007, p. 78–81), we implement two tests to remove such spurious numerical modes.

The first condition requires that the eigenvalues do not move significantly when the numerical discretization is changed. Suppose eigenvalues  $\{\omega_p\}$  have been computed using a discretization  $(N_x, N_y)$ , and suppose  $\{\hat{\omega}_q\}$  have been computed with a slightly increased resolution, such as  $(N_x + 1, N_y + 1)$ . The first condition is then given by requiring that, for each eigenvalue  $\omega_p$ ,

$$\min_q |\omega_p - \hat{\omega}_q| < \text{tol}, \tag{A 11}$$

where  $\text{tol}$  is a prescribed tolerance. For the results computed in this paper  $\text{tol} = 10^{-2}$  was used.

The second resolvedness condition involves the spectral coefficients of the eigenfunctions. In particular, we require the modulus of the spectral coefficients to decay smoothly as the number of polynomials used gets larger. Both the aforementioned conditions have been applied to the pressure eigenfunctions as this is the unknown of most interest because it contains information on the shape of the free surface height. So, let  $\phi_{ij}$  be a generic spectral coefficient, the following condition has been implemented

$$\frac{\sup_{(i,j) \in \mathcal{B}} |\phi_{ij}|}{\sup_{\text{all } i,j} |\phi_{ij}|} < \text{tol}, \tag{A 12}$$

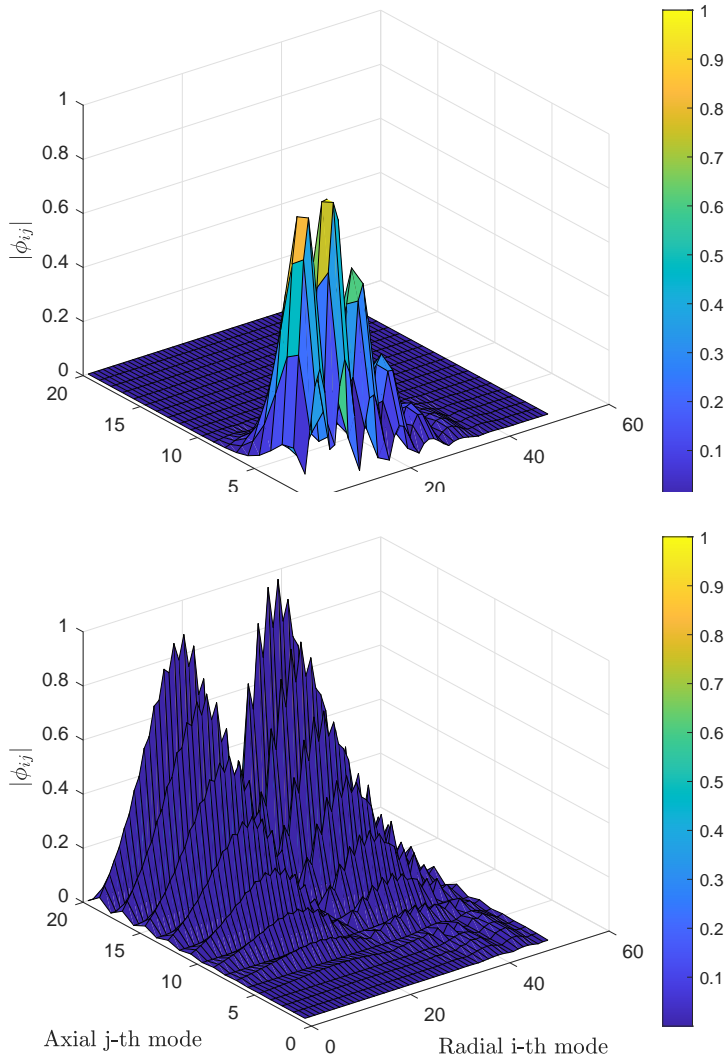


FIGURE 13. Example of a well-resolved mode (Top) and a poorly-resolved mode (Bottom).

where  $\mathcal{B}$  is a part of the domain in the  $N_x - N_y$  plane, defined as

$$\mathcal{B} = \{(i, j) : N_x + 1 - b_x \leq i \leq N_x + 1 \text{ or } N_y + 1 - b_y \leq j \leq N_y + 1\}, \quad (\text{A } 13)$$

tol is a prescribed tolerance on the magnitude of the coefficients and  $b_x, b_y$  two prescribed borders widths in the  $N_x - N_y$  plane. Figure 13 compares the magnitude of the coefficients for a well resolved mode and a poorly-resolved mode for  $N_x = 50$ ,  $N_y = 20$ ,  $b_x = 12$ , and  $b_y = 4$ ,  $\text{tol} = 10^{-1}$ . The well-resolved mode can be seen to have spectral coefficient  $|\phi_{ij}|$  decreasing exponentially quickly. By contrast, for the poorly-resolved mode, the spectral coefficients  $|\phi_{ij}|$  are oscillatory increasing as function of the number of polynomials used.

## REFERENCES

- BAYLISS, A. & TURKEL, E. 1980 Radiation boundary conditions for wave-like equations. *Communications on Pure and Applied Mathematics* **33**, 707–725. doi: 10.1002/cpa.3160330603.

- BERENGER, J. P. 1994 A perfectly matched layer for the absorption of electromagnetic waves. *J. Comput. Phys.* **114**, 185–200. doi: 10.1006/jcph.1994.1159.
- BRAMBLEY, E. J. 2007 The acoustics of curved and lined cylindrical ducts with mean flow. PhD thesis, University of Cambridge. doi: 10.17863/CAM.16086.
- BRAMBLEY, E. J. & PEAKE, N. 2008 Sound transmission in strongly curved slowly varying cylindrical ducts with flow. *J. Fluid Mech.* **596**, 387–412. doi: 10.1017/S0022112007009603.
- DRAZIN, P. G. & RILEY, N. 2006 *The Navier-Stokes equations: a classification of flows and exact solutions*. Cambridge University Press. ISBN 9780521681629.
- ENGQUIST, B. & MAJDA, A. 1977 Absorbing boundary conditions for the numerical simulation of waves. *Mathematics of Computation* **31**, 629–651. doi: 10.1090/S0025-5718-1977-0436612-4.
- FRITZ, J. 1978 *Partial differential equations*. Springer Verlag. ISBN 9781468400618.
- GREENSPAN, H. P. 1969 *The theory of rotating fluids*. Cambridge University Press. ISBN 9780521051479.
- GROTE, M. J. 2000 Non-reflecting boundary conditions for time dependent wave propagation. *Research Report/Seminar für Angewandte Mathematik* doi: 10.3929/ethz-a-004288373.
- GROTE, M. J. & KELLER, J. B. 1995 Exact nonreflecting boundary conditions for the time dependent wave equation. *SIAM J. Appl. Math.* **55**(2), 280–297. doi: 10.1137/S0036139993269266.
- HUNT, M. 2019 Two-dimensional surface waves in magnetohydrodynamics. *J. Plasma Phys* **85**. doi: 10.1017/S0022377819000497.
- HUNT, M., PARAU, E., VANDEN-BROECK, J.-M. & PAPAGEORGIOU, D. 2015 Linear and nonlinear surface waves in electrohydrodynamics. *arXiv* :**1501.02783**. doi: 10.48550/arXiv.1501.02783.
- HUNT, M. J. & DUTYKH, D. 2021 Free surface flows in electrohydrodynamics with a constant vorticity distribution. *Water Waves* **3**, 297–317. doi: 10.1007/s42286-020-00043-9.
- HUNT, M. J. & VANDEN-BROECK, J.-M. 2015 A study of the effects of electric field on two-dimensional inviscid nonlinear free surface flows generated by moving disturbances. *Journal of Engineering Mathematics* **92**, 1–13. doi: 10.1007/s10665-014-9766-6.
- JOHNSON, R. S. 1997 *A Modern Introduction to the Mathematical Theory of Water Waves*. Cambridge University Press. ISBN 9780521598323.
- KELLER, J. B. & GIVOLI, D. 1989 Exact non-reflecting boundary conditions. *Computational Physics* **82**, 172–192. doi: 10.1016/0021-9991(89)90041-7.
- LINDQUIST, J. M., NETA, B. & GIRALDO, F. X. 2012 High-order non-reflecting boundary conditions for dispersive waves in polar coordinates using spectral elements. *Applied Mathematics and Computation* **218**, 6666–6676. doi: 10.1016/j.amc.2011.12.023.
- MCWILLIAMS, J. C. 2006 *Fundamentals of Geophysical Fluid Dynamics*. Cambridge University Press. ISBN 978052185637.
- MOUGEL, J., FABRE, D. & LACAZE, L. 2014 Waves and instabilities in rotating free surface flows. *Mechanics and Industry* **15**, 107–112. doi: 10.1051/meca/2014007.
- MOUGEL, J., FABRE, D. & LACAZE, L. 2015 Waves in newton’s bucket. *J. Fluid Mech.* **783**, 211–250. doi: 10.1017/jfm.2015.527.
- MOUGEL, J., FABRE, D., LACAZE, L. & BOHR, T. 2017 On the instabilities of a potential vortex with a free surface. *J. Fluid Mech.* **824**, 230–264. doi: 10.1017/jfm.2017.341.
- PATRICK, S. 2019 On the analogy between black holes and bathtub vortices. PhD thesis, School of Mathematical Sciences - University of Nottingham.
- PATRICK, S., COUTANT, A. & RICHARTZ, M. 2018 Black-hole quasibound states from a draining bathtub vortex flow. *Physical Review Letters* **121**. doi: 10.1103/PhysRevLett.121.061101.
- QUARTERONI, A. 2009 *Numerical models for differential problems*. Springer-Verlag Italia. ISBN 9788847010710.
- SIM, I. 2010 Non-reflecting boundary conditions for time-dependent wave propagation. PhD thesis, University of Basel. doi: 10.5451/unibas-005269594.
- SKIPP, J. M. 2020 Single vortex ring. <https://youtube.com/shorts/ApwCq7UkCfY>, accessed 2021-11-09.
- WELLENS, P. & BORSBOOM, M. 2019 A generating and absorbing boundary condition for dispersive waves in detailed simulations of free-surface flow interaction with marine structures. *Computers and Fluids* **200**. doi: 10.1016/j.compfluid.2019.104387.